Lifetime spectroscopy with high spatial resolution based on temperature- and injection dependent photoluminescence imaging

Halvard Haug[1 *], Rune Søndenå[1], Amalie Berg[1] and Marie Syre Wiig[1]

1 Institute for Energy Technology, Instituttveien 18, 2007 Kjeller, Norway.

Abstract

In this paper we present a method for performing temperature- and injection dependent lifetime spectroscopy (TIDLS) with high spatial resolution based on steady state photoluminescence (PL) images taken at a range of excitation intensities and temperatures. The PL lifetime images are calibrated based on temperature dependent photoconductance measurements, thus requiring a minimum of assumptions regarding the temperature dependency of the luminescence signal and detection system. PL image acquisition at varying conditions and subsequent data analysis is automated, allowing for investigations of different samples without the need for excessive operator time. We demonstrate the method by presenting lifetime data and TIDLS analysis from commercial HPMC-Si samples, highlighting the local differences in the recombination properties for high lifetime in-grain areas and lower lifetime areas dominated by dislocation clusters. These regions have been investigated for two etched and passivated neighboring wafers, one in the as-cut state and one were the bulk lifetime had been improved through key solar cell process steps. For the as-cut wafer we find two dominant defects in the low lifetime area, one of which is identified as FeB pairs, with $E_t = 0.90 \pm 0.01$ (above the valence band) and $k = 0.4 \pm 0.1$. In the in-grain region of this wafer we also observe two dominating defects, one with an energy level of either 0.28 ± 0.01 eV or 0.74 ± 0.01 eV above the valence band and a k value of 25 ± 1. The other defect is shallow, within ~0.27 eV of the band edge, and could not be further identified with the chosen temperature range. For the wafer that had passed through solar cell processing, we find a clear, overall improvement in the lifetime and a change in the type of dominating defects: We observe that a single, deep defect with $0.35\ eV < E_t < 0.7\ eV$ and a capture cross section ratio $k = 10 \pm 1$ can fully describe the observed lifetime data in the in-grain area after solar cell processing, whereas two defects are needed to describe the behavior of the lower lifetime regions. One of these defects is also a deep defect with $0.34\ eV < E_t < 0.69\ eV$ but with a higher k of 25 ± 2, and is thus similar to one of the defects observed in the in-grain region of the as-cut wafer. The other is a shallow defect with E_t within $0.21\ eV$ of the band edge. Finally, we show how the method can be used to show interesting new properties of the lifetime maps, including maps of the temperature coefficient of the lifetime, maps of the injection dependence of the lifetime and maps at a constant injection level.

Keywords: Multicrystalline silicon, Photoluminescence, Lifetime spectroscopy, Recombination, Defects

1. Introduction

The minority carrier lifetime is the key parameter determining the material quality of crystalline silicon (c-Si) wafers for solar cells, and in most cases it directly affects the efficiency of the final solar cell. Recombination of electron-hole pairs through defect levels in the band gap of silicon, called Shockley-Read-Hall-recombination (SRH), is normally the most important recombination process in the bulk material limiting the carrier lifetime, and can be a significant source of efficiency loss in both monocrystalline Czochralski (Cz) and multicrystalline Si. For the case of Cz silicon the lifetime can be reduced by the presence of different metallic impurities, but also by intrinsic defects such as vacancies and silicon self-interstitials as well as oxygen-related defects and complexes thereof [1]. Oxygen-related defects that can act as recombination centers include thermal donors,

boron-oxygen complexes, and oxygen precipitates, the latter oxygen precipitates may grow to induce stacking faults in the crystal lattice [2]. For the case of multicrystalline silicon, the main losses are related to extended crystal defects, such as grain boundaries and dislocation clusters, in addition to impurities. These crystal defects are not necessarily harmful to the carrier lifetimes, but they tend to be decorated with impurity species forming detrimental recombination sites [3]. Most leading producers of multicrystalline Si ingots and wafers in the PV industry have converted their production processes to fabricate so-called high-performance multicrystalline Si (HPMC-Si) material. These wafers feature smaller grains, which strongly inhibits formation of the very detrimental dislocation clusters, which have led to a significant increase in solar cell efficiency.

The lifetimes in intragrain regions of a HPMC-Si wafer are in many cases no longer inferior to the lifetimes in Cz-Si wafers, suggesting that the solar cell efficiency of HPMC-Si cells is unlikely to be limited by the intragrain regions [4]. In addition to this, there are several recombination mechanisms responsible for degradation in both Cz and HPMC-Si solar cells, and fundamental knowledge of the recombination processes and how to manipulate the defect states is therefore important. Light induced degradation (LID) related to boron-oxygen complexes is widely studied in mono-Si has also been observed in HPMC-Si as the general impurity levels have been reduced [5], [6]. The so-called light and elevated temperature induced degradation (LeTID) and regeneration is also an evident effect mostly observed on HPMC-Si [7]. The recombination states and reaction rates of these defects can be affected by illumination, carrier injection and heat. This difference between Cz-Si and HPMC-Si, together with small differences in optical properties, results in a current efficiency gap of about 1.5 $\%_{absolute}$ in favor of Cz-Si solar cells [8]. A detailed understanding of the fundamental properties of defect formation and the fundamental properties of recombination active defects is vital to avoid or mitigate the effects of defects during crystal formation, both in Cz-Si and in HPMC-Si. The lifetime may then also considerably altered during the solar cell process, especially during high temperature steps. Most importantly, phosphorus diffusion gettering removes more than 90% of the metallic impurities in multicrystalline silicon, and certain types of grain boundaries might also later be passivated by hydrogen during contact firing [9] [10] [11] [12].

In order to study and understand the electronic properties of limiting defects in Si it is necessary to decouple the recombination processes arising from e.g. metallic impurities, defect complexes and extended crystal defects from each other, thus identifying the specific signatures of each recombination mechanism. A sophisticated analysis method is therefore necessary to separate the signatures of the different recombination paths. Temperature and injection dependent lifetime spectroscopy (TIDLS) is a well-established method, and is in many cases the only method available with sufficient sensitivity to detect small concentrations of detrimental impurities and other defects in Si. TIDLS has previously often been used to identify the recombination signatures of known impurities using intentionally contaminated samples.

Photoluminescence (PL) imaging is a commonly used method for measuring the spatial distribution of the carrier lifetime in c-Si wafers. Several groups have worked towards developing methods for performing TIDLS [13]–[15] with high spatial resolution [16]–[19]. Such measurements have previously been performed by harmonically modulated PL, but this requires expensive and often custom-built setups with a time resolved PL detection system. In this work we demonstrate lifetime spectroscopy analysis based on a large number of images automatically acquired at different conditions using a conventional steady state PL imaging tool. We use these images together with suitable post-processing software for performing spatially resolved TIDLS analysis, as well as studying fundamental temperature- and injection level-dependent properties of silicon wafers.

2. Temperature- and injection dependent lifetime spectroscopy

SHR recombination centers give rise to a specific behavior of the lifetime as a function of excess carrier density (injection level) and temperature, which is characteristic of the defect or impurity dominating the recombination process. Temperature and injection dependent lifetime spectroscopy is therefore a powerful tool for identification of the SRH recombination centers limiting the lifetime in the material, and for quantification of their relative concentrations [13]. It can also be used to identify defect specific recombination parameters by analyzing materials with known dominating recombination centers [14], [15], [20]–[22].

To isolate the lifetime due to SRH recombination centers the effective lifetime data should be corrected for intrinsic recombination, here this is done according to the model of Richter et al. [23]. In the case of p-type Si and a single dominating SRH defect, the SRH lifetime should take a linear form when represented as a function of the electron to hole ratio *X* [24], given by

$$X = \frac{n}{p} = \frac{\Delta n}{N_A + \Delta n}. \tag{1}$$

If two defects are both influencing the total lifetime, the SRH lifetime can be represented as the inverse sum of two linear expressions, given by

$$\frac{1}{\tau_{eff,SRH}} = \frac{1}{\tau_{0n,1}(a_1(T)X + b_1(T))} + \frac{1}{\tau_{0n,2}(a_2(T)X + b_2(T))}, \tag{2}$$

where τ_{0n} is the SRH parameter for minority carriers for each of the two defects, defined as $\tau_{0n} = 1/(N_t \sigma_n v_{th})$, where N_t is the defect concentration, σ_n is the capture cross section for electrons and v_{th} is the thermal velocity of the carriers. *a(T)* and *b(T)* are temperature dependent linear coefficients. This linear parameterization greatly simplifies the separation of the SRH lifetime due to two independent defects. After separating the SRH lifetime from each of the two defects, a defect parameter solution surface (DPSS) can be calculated independently for both defects at each temperature [13]. A DPSS at a single temperature spans out all combinations of E_t and k which can describe the current lifetime curve. However, DPSS's obtained at different temperatures will ideally have only two common points, where the curves intersect, isolating two pairs of E_t and k describing the current defect, one in each half of the band gap. For a further description of the TIDLS method, see Refs. [13], [17], [18], [24].

3. Experimental details

3.1 Sample preparation

The investigated wafers were processed in IFEs solar cell line, with the aim of evaluating the bulk lifetimes at different stages in the solar cell production process. Two neighboring wafers were processed for the investigations in this work: Wafer A, called *as-cut*, has not been subjected to any high temperature processing steps after the casting process. It has, however, been damage etched in an HNA-solution (HF : HNO_3 : CH_3COOH). The second sample is subjected to high temperature profiles comparable to the ones used in a commercial solar cell process: A dual side phosphorus emitter in-diffusion were performed in a Tempress tube furnace using $POCl_3$ gas as the dopant source, forming an emitter of approximately 75 Ωcm. Subsequently, a simulated firing process was performed in a belt furnace after application of a hydrogen rich SiN_x:H anti-reflection coating (ARC) present on both sides of the wafer. No metal contacts were applied prior to the firing. ARC's and emitters were removed in a new HNA-solution before the wafers were cleaned and surface passivated with an a-Si:H/SiN_X:H stack deposited on both sides using plasma enhanced chemical vapor deposition (PECVD) in an Oxford Plasmalab 133 chamber. Surface recombination velocities of less than 5 cm/s are routinely obtained using this passivation scheme [25]. Prior to lifetime measurements the wafers were light soaked with about 20 mW/cm^2 (LED) for 72 hours at room temperature to stabilize any degradation caused by boron-oxygen defects. A process flow chart illustrating the sample processing of the two wafers is shown in Figure 1.

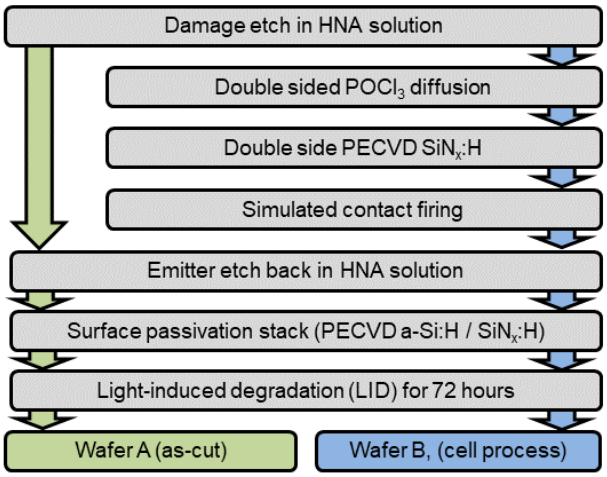

Figure. 1. The process route for the two different wafers investigated in this work. The process is designed to produce lifetime samples with low surface recombination velocity (SRV) for minority carrier lifetime measurements, and where the bulk lifetime is similar to that of as-cut wafers (A), and as close as possible to that of final solar cells (B).

3.2 Temperature- and injection level PL image acquisition

Uncalibrated PL intensity images were recorded as a function of temperature using a heating stage built into a LIS-R1 PL imaging setup from BT imaging with a laser excitation wavelength of 808 nm. A short-pass filter was used in front of the camera to strongly reduce the parts of the luminescence signal originating from deep within the wafer, including the signal that is reflected from the rear side of the sample, to reduce smearing effects from lateral carrier diffusion. Images were measured in 10 ˚C intervals from 25 to 75 ˚C. Temperatures exceeding 75 ˚C were not used to avoid any permanent annealing effects of the samples, such as lifetime regeneration after light induced degradation (LID) related to boron-oxygen defects or iron-boron pair formation. Such annealing effects were ruled out in each case by performing a reference quasi-steady state photoconductance (QSSPC) measurement at room temperature before and after each temperature scan.

An automated measurement routine was used to simplify the acquisition of the PL images at different measurement conditions. 30 images were acquired at each temperature using a range of laser excitation intensities corresponding to generation rates in the range between $G = 1.2 \times 10^{18}$ and 2.2×10^{20} $cm^{-3}s^{-1}$, thus covering a large part of the injection range of interest. In order to obtain high injection data also from low lifetime areas, half of the images were measured using the option in the LIS-R1 setup for smaller area illumination, were the laser power is more focused to reach higher photon flux values. To ensure correct quantification for both large and small area settings, an independent reference measurement of the optical power was undertaken. A small offset was observed when using the same flux with the large and small area settings, and this difference was therefore corrected in post-processing in order to obtain smooth transitions in the overlapping region. For all images the signal to noise ratio was kept at the desired level by adjusting the integration time of the camera detection system according to the excitation photon flux in each case. A schematic illustration of the experimental setup is shown in Figure 2.

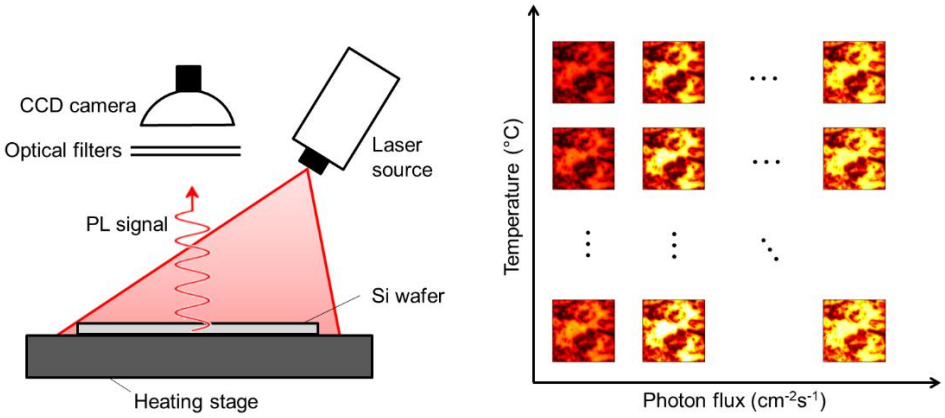

Figure 2. Schematic illustration of the measurement setup (left), using a heating stage within a PL imaging setup. In this paper PL images of each sample are acquired at 6 different temperatures, with 30 different values of the excitation photon flux for each temperature, as shown schematically in the right-hand side of the figure.

3.3 Temperature dependent calibration of PL lifetime images

The measured intensity I_{PL}, here defined in counts registered by the camera per second, is given by

$$I_{PL} = C\left(np - n_i^2\right) \approx C\Delta n\left(N_{dop} + \Delta n\right), \quad (3)$$

where n and p is the electron and hole densities, N_{dop} is the dopant concentration (n- or p-type) and Δn is the injection level. C is an instrument- and sample-dependent calibration constant, which includes the radiative recombination coefficient of Si B_{rad}, the optical properties of the sample, the geometry of the measurement setup, signal reduction due to filters, etc. Normally PL lifetime images at room temperature are calibrated based on a secondary photoconductance measurement to determine the value of C. However, the calibration constant is generally temperature dependent, decreasing as a function of increasing temperature. This is caused by the fact that the band-to-band luminescence peak of crystalline Si is lowered and shifted to higher wavelengths as the temperature increases. This peak is then detected using a Si CCD camera, which therefore have a strongly spectrally dependent sensitivity of the in the wavelength range around the luminescence peak [26]. The use of additional filters, like the short-pass filter used here to reduce smearing effects from lateral diffusion, complicates matters further. It is in principle possible to account for all these effects theoretically to determine a temperature-dependent calibration procedure, as done in Ref. [27], but the added complexity introduces several uncertainties in the quantification of the carrier lifetime. Instead, we have here used the same approach we previously introduced in Ref. [25], using a temperature-dependent quasi-state-state photoconductance setup to perform the conventional calibration procedure based on a separate QSSPC measurement at each temperature.

To obtain the necessary calibration constants, minority carrier lifetime curves were measured as a function of injection level at a range of temperatures using a Sinton WCT-120 TS lifetime tester. The injection level Δn is here calculated from the photoconductance, which is measured by an inductive coil built into a temperature-controlled sample stage. A temperature dependent mobility model is need for this purpose, here the model of Dorkel and Leturcq is used [28]. The setup provides an unique opportunity to quantitatively measure the carrier lifetime as a function of both injection level and temperature, with a possible measurement range from 25 to 200 °C [29]. In the same way as for the PL images, the maximum temperature was set at a sufficiently low value to avoid permanent annealing effects. Careful temperature measurements of both heating stages were performed to minimize differences between the two setups. All measurements were automatically saved in raw data form together with the key measurement conditions, and the full calibration procedure and subsequent calculations, plotting and data analysis was then performed using an in-house MATLAB code library written for this purpose.

It has previously been shown that calibration of PL images can be significantly influenced by lifetime non-uniformities in the measurement region over the PC coil [30]. Lifetime spectroscopy requires high precision in the effective lifetime data, and the temperature dependent QSSPC measurements were therefore performed on an as homogeneous area of the sample as possible to minimize quantification errors. Because the investigated wafers are multicrystalline, all such non-uniformities could, however, not be avoided.

The carrier lifetime images were finally calculated based on similar algorithms used for room temperature measurements [31]: For each temperature and generation rate, the calibration constant C was calculated from Eq. (3) based on the Δn value taken from the appropriate point of the QSSPC

curve and the PL intensity I_{PL} taken from the PL image in a region between two concentric rings around the PC coil. Ideally, we expect the calibration constant to be independent of injection level and thus of the generation rate. After all, this is a central assumption of the PL imaging method: The entire lifetime image, which consist of regions of different injection level, is calculated based on a single calibration constant determined from these two local measurements. However, in many cases we find that the calibration constant is not entirely independent on injection level, as shown in Figure 3 a). This is caused by a difference in the injection dependence measured using QSSPC and PL, which might be caused by e.g. carrier trapping in the photoconductance measurements [32], or by the abovementioned lifetime non-uniformities in the coil area. In any case, we approach this problem by averaging the measured calibration constants in a mid-level injection range. The average calibration constant is shown as a function of temperature in Figure 3 b), with the error bars indicating the standard deviation within each temperature. The results are observed to follow a linear trend, and a linear regression of these data were used to calculate a single calibration constant for all the PL images which is linearly dependent on temperature. By inserting this calibration constant $C(T)$ into Eq (3) and solving for Δn, the steady state effective lifetime $\tau_{eff} = \Delta n/G$ at each point of the lifetime image is then calculated as for each temperature T and excitation flux ϕ_{ph}:

$$\tau_{eff}(T,\phi_{ph}) = \frac{\Delta n(T,\phi_{ph})}{G(\phi_{ph})} = \frac{1}{G(\phi_{ph})}\left(\sqrt{\left(\frac{N_{dop}}{2}\right)^2 + \frac{I_{PL}(T,\phi_{ph})}{C(T)}} - \frac{N_{dop}}{2}\right) \quad (4)$$

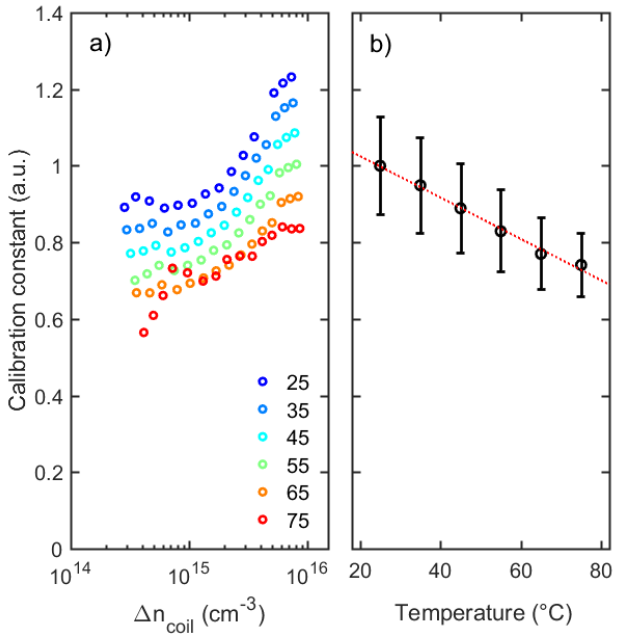

Figure 3. a) Normalized calibration constants calculated at different injection levels for the large area illumination images. Each value is calculated from the appropriate calibration point on the measured temperature dependent QSSPC curve and from the uncalibrated PL data taken from a donut-shaped region around the photoconductance coil. As exemplified here, we do generally not observe the calibration constant to be perfectly constant with injection level. b) Average calibration constant (black circles) as a function of temperature, with error bars indicating the standard deviation within each temperature. The calibration constant was found to decrease linearly with temperature. A linear regression of these data (red dotted line) was used to calibrate the PL images.

4. Results and discussion

4.1 Carrier lifetime images and the effect of solar cell processing

Conventional PL images measured at 25 ˚C and an excitation flux of $\phi_{ph} = 1.02 \times 10^{17}$ cm^{-2}s^{-1} are shown for both Wafer A (as-cut) and Wafer B (after cell processing) in Figure 4. Because of the need for small area illumination to obtain sufficiently high injection levels in low lifetime regions, only a part of the complete 6-inch wafers were analyzed (see length scale). Because the wafers are selected from the top part of the cast, they are dominated by larger grains and dislocation clusters [33]. This was purposefully selected to simplify the use of the local analysis without too much influence from lateral diffusion (see discussion below). We observe a clear improvement in the bulk lifetime after gettering and hydrogenation, with in-grain lifetimes improving from ~100 µs to ~700 µs after processing (note the different color scale in the lifetime images).

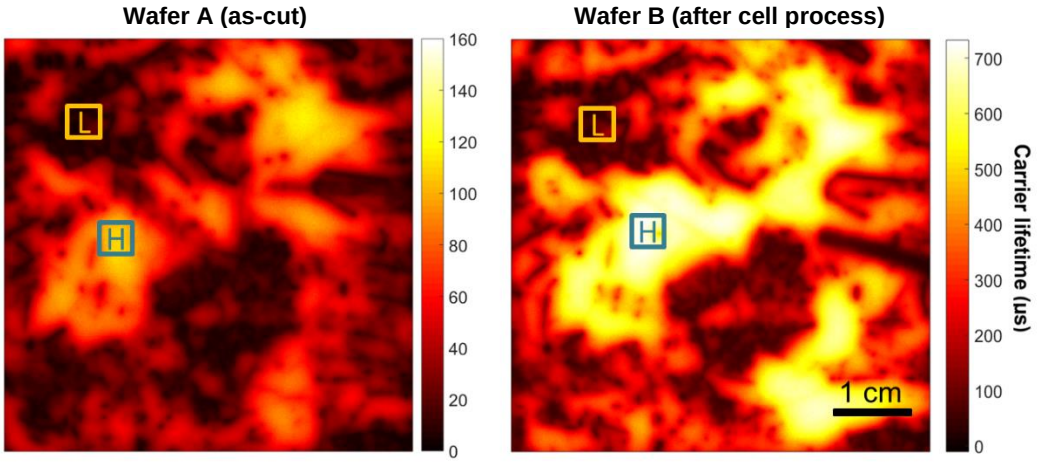

Figure 4. Lifetime images acquired at 25 ˚C and a constant excitation flux of 1.02×10^{17} cm^{-2}s^{-1}, acquired from wafer A (left) and Wafer B (right). As expected, the overall lifetime is observed to clearly improve after gettering and hydrogenation. Note the different scales on the two images.

4.2. Local TIDLS analysis

Two regions, one from the middle of a large grain with high lifetime (marked with [H]) and one from a region dominated by dislocation clusters (marked with [L]) were selected for further analysis, as indicated in Figure 4. Temperature- and injection dependent effective lifetime curves were found by averaging the lifetime in each region for each of the 180 images measured on each sample (corresponding to 6 temperatures and 30 photon flux values). These lifetime curves were then used for further lifetime spectroscopy analysis, as shown in Figure 5 and Figure 6 for wafers A and B, respectively. For each wafer, subfigures a) and d) show the experimental effective carrier lifetime as function of injection level at different temperatures for the high lifetime and low lifetime regions, respectively. The observed lifetime behavior is both qualitatively and quantitatively different at the different regions, and the behavior is also strongly dependent on the wafer processing. In all cases the modelled curves obtained from the best-fit parameters show an excellent agreement with the experimental data. To isolate the lifetime due to SRH recombination centers the measured effective lifetime data was corrected for intrinsic recombination according to the model of Richter et al [23]. As described in Section 2 above, the SRH lifetime is then linearized by plotting it against the electron to hole concentration ratio, X, as shown in b) and e). For the high lifetime region of Wafer B (Figure 6 b), the SRH lifetime is clearly linear with X, indicating that the measured data is dominated by a single SRH defect level. For the other investigated regions, this linearization was followed by a fit of the inverse sum of two linear curves (as described by Eq. 2 above), indicating that two defects are required to appropriately fit the experimental data. Subfigures c) and f) in Figures 5 and 6 show the DPSS curves for the two defects observed in each region, with the solutions space of all possible pairs of E_t and k which give an equally good fit to the experimental data at each temperature. The bottom part of c) and f) show the root mean square difference between all k values at different temperatures as a function of E_t, and minima in these curves, therefore, represent the best fit values. A detailed view of the points of intersection between the DPSS curves obtained at different temperatures is shown in subfigure g). These common solutions are then used to determine E_t and k for each defect, as discussed below. In some cases, no clear crossing points are observed between the DPSS curves, which we assume is caused by inaccuracies in the measurement procedure or possibly from a temperature-dependent k parameter for these defects.

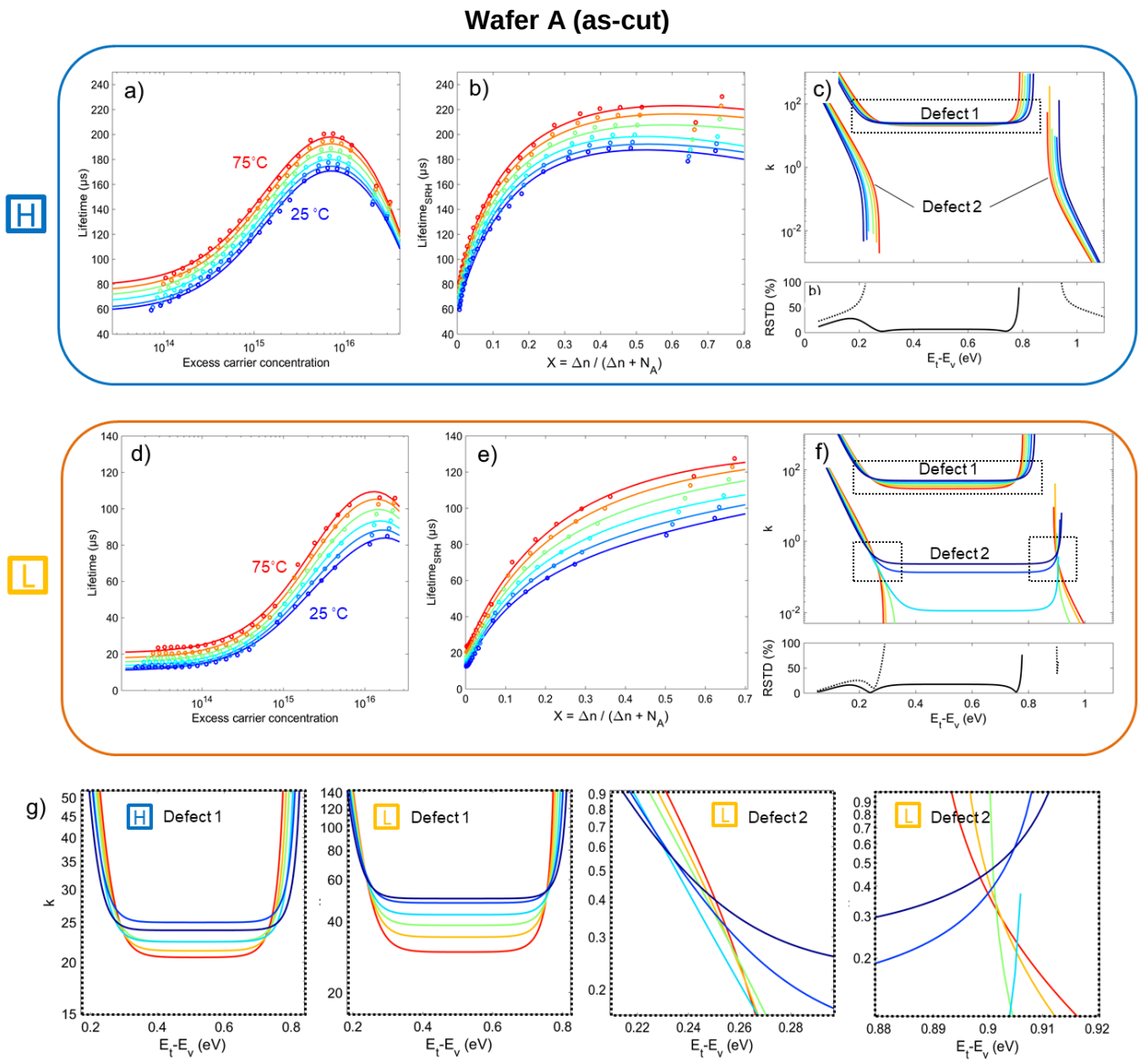

Figure 5. Image-based TIDLS analysis based on PL data measured and on the as-cut wafer (Wafer A). Local analysis is shown from two different regions of the wafer, [H] is from a high lifetime area (middle of a large grain) and [L] is from a low lifetime region dominated by dislocation clusters, as indicated in Figure 4.

a) and d) show the average temperature- and injection dependent carrier lifetime for regions [H] and [L] respectively. Open circles indicate experimental data (each point representing the average of the current area in a lifetime image), and lines show the best-fit TIDLS model of the data.

b) and e) show the linearization of the lifetime by plotting it against X=n/p. A single SRH defect is expected to be linear in this form. For the case of two defects the defects are separated by fitting an inverse sum of two linear curves, according to Eq. (2).

c) and f) show the defect parameter solution space (DPSS) obtained from each of the best fit defects, showing the solution space in E_t and k at each temperature. Colors are used to indicate different temperatures between 25 ˚C (blue) and 75 ˚C (red). The bottom parts of c) and f) show the relative standard deviation in the k values at different temperatures, thus indicating energy regions which give good solution for all temperatures.

g) Different zoomed in regions of the DPSS curves, as indicated by dotted squares in c) and f), showing the crossing points where we find common solutions for all temperatures for Defect 1 in the high lifetime region and for Defects 1 and 2 in the low lifetime region.

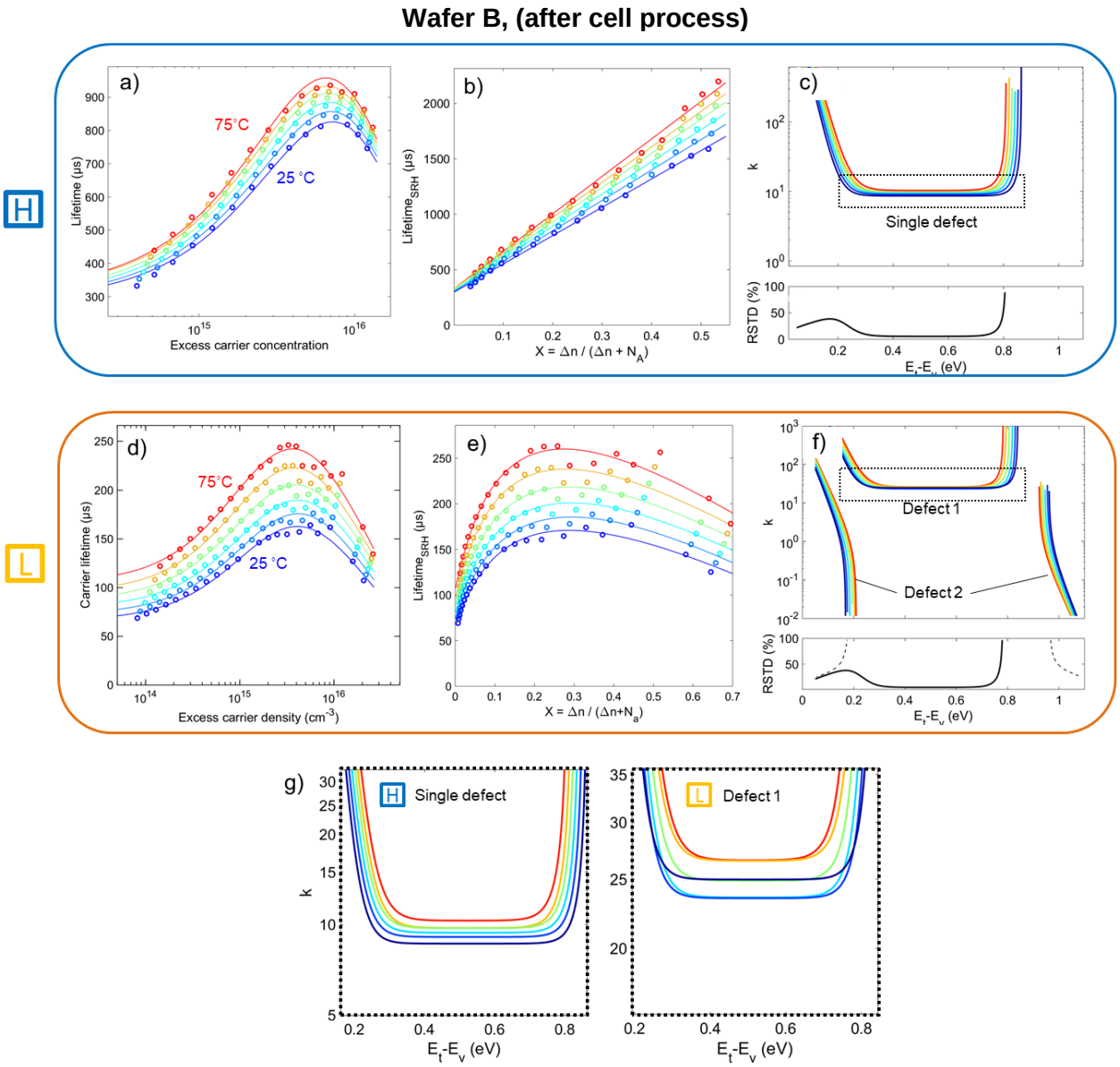

Figure 6. Image-based TIDLS analysis based on PL data measured and on the wafer after simulated solar cell processing (Wafer B). Local analysis is shown from two different regions of the wafer, [H] is from a high lifetime area (middle of a large grain) and [L] is from a low lifetime region dominated by dislocation clusters, as indicated in Figure 4.

a) and d) show the average temperature- and injection dependent carrier lifetime for regions [H] and [L] respectively. Open circles indicate experimental data (each point representing the average of the current area in a lifetime image), and lines show the best-fit TIDLS model of the data.

b) and e) show the linearization of the lifetime by plotting it against X=n/p. A single SRH defect is expected to be linear in this form. For the case of two defects the defects are separated by fitting an inverse sum of two linear curves, according to Eq. (2).

c) and f) show the defect parameter solution space (DPSS) obtained from each of the best fit defects, showing the solution space in E_t and k at each temperature. Colors are used to indicate different temperatures between 25 ˚C (blue) and 75 ˚C (red). The bottom parts of c) and f) show the relative standard deviation in the k values at different temperatures, thus indicating energy regions which give good solution for all temperatures.

g) Zoomed in regions of the DPSS curves, highlighting the single defect observed in the high lifetime region and Defect 1 in the low lifetime region, as indicated by dotted squares in c) and f). No clear crossing points are observed in this wafer, which is most probably caused by a deep defect with a slightly temperature dependent k.

Table I. Defect parameters observed in this work

Wafer	Region	Defect	Lower band gap		Upper band gap	
			E_t (eV)	k	E_t (eV)	k
A (as-cut)	H (in-grain)	1	<0.27	-	> 0.89	-
		2	0.28 ± 0.01	25 ± 1	0.74 ± 0.01	25 ± 1
	L (dislocations)	1	0.25 ± 0.01	0.4 ± 0.1	0.90 ± 0.01	0.4 ± 0.1
		2	0.24 ± 0.01	62 ± 1	0.75 ± 0.01	53 ± 1
B (after cell process)	H (in-grain)	Single	0.35 - 0.7	10 ± 1	(assumed deep defect)	
	L (dislocations)	1	< 0.21	-	> 0.92	-
		2	0.34 - 0.69	25 ± 2	(assumed deep defect)	

Recombination parameters identified in an in-grain (H) and a dislocated (L) region for from each of the two samples are listed in Table I. For wafer A (as-cut) the defect parameters for three out of four defect levels could be accurately determined where the DPSS curves had a common point of intersection. The capture cross sections in the dislocated area are close to those previously reported for FeB and Fe_i. The energy level for the defect with a capture cross section of $k = 0.4 \pm 0.1$ is located at $0.25\ eV$ or $0.90\ eV$, we attribute this to FeB previously found at $0.89 \pm 0.03\ eV$ with at capture cross section of 0.45 [21]. As the samples are illuminated during PL-imaging a partly dissociation of FeB and a following presence of Fe_i is therefore expected. Even though the $k = 51 \pm 1$ corresponds well with literature values for Fe_i ($k = 51 \pm 5$), the energy level located at $E_t = 0.24$ or $0.75\ eV$ are not consistent with literature values for Fe_i at $E_t = 0.394 \pm 0.005$ [21]. We can therefore not conclude further about the identification of the observed defect level based on this. The in-grain area (H) of Wafer A has one defect level at $E_t = 0.28$ eV or $E_t = 0.74$ eV with $k = 25$, and one shallower defect with a definition gap between $0.27\ eV < E_t < 0.89$ eV. No common point of intersection was observed for this last defect, hence exact recombination parameters for E_t and k could not be determined.

The dislocated area (L) of wafer B (after cell process) shows similar defect parameters to the in-grain region of wafer A. Defect 1 is a deep defect with $k = 25 \pm 2$ and the second defect has a definition gap between $0.34\ eV < E_t < 0.69$ eV. However, the position of the energy levels is inaccurate due to lack of a common intersection between the DPSS curves. Only one dominating recombination center is observed in the in-grain region (H) of Wafer B. This single defect has $0.35\ eV < E_t < 0.7\ eV$ and $k = 10 \pm 1$. Due to the lack of a point of intersection in the DPSS this recombination centre has not been attributed a single defect.

We have in this case limited our defect identification to a two-defect case to ensure unique solutions, as a three-defect fit as used in eg. Ref. [17] require a pre-assumption on which defects that are present. Mapping of defect parameters from temperature dependent PL-images has previously been shown in [18], however, the two approaches to extract defect parameters are slightly different. The current analysis identifying the exact defect parameters is pending on identification of an intersection between the DPSS curves which is difficult to obtain in regions with more than two defects with similar recombination activity, or in the case of a temperature dependent k. Hence in this work evaluation of local relatively uniform areas was preferred prior to global mapping of the whole wafer. However, the methodology can be extended to produce a concentration map of areas where one or two selected defects dominates the recombination.

4.3. Advanced carrier lifetime image visualization

After the matrix of images with flux- and temperature variations is imported into Matlab it is of course possible to visualize this information in other ways than what is shown in Figures 5 and 6. Another option is to plot the different trends in temperature and injection level dependence in image form. One useful metric in this regard is the temperature coefficient for the carrier lifetime TC_τ, defined as

$$TC_\tau = \frac{100\%}{\tau_{25\,^\circ C}} \times \frac{d\tau}{dT}, \tag{5}$$

where $\tau_{25\,^\circ C}$ is the lifetime at 25 ˚C and $d\tau$ is the change in lifetime over the temperature interval dT. The TC_τ for Wafer B, taken at a constant exciation flux of $\phi = 1.02 \times 10^{17}$cm^{-2}s^{-1}, is shown in Figure 7. By comparing with Figure 4, we see that there is a clear correlation between low lifetime (dislocation dominated) areas and areas of high TC_τ (high relative improvement in the carrier lifetime with increasing temperature), which was also recently observed by Eberle et al in both multicrystalline wafers and cells [34]. This is not only a consequence of the low lifetime itself: Notice the horizontal feature of low lifetime at the middle of the right edge of Figure 4, which is almost not visible in the TC_τ map. We can therefore conclude that this recombination in this region has a different origin, most probably due to surface damage.

Another option for visualizing the data is by plotting the relative change in carrier lifetime with increasing photon flux, as shown in Figure 8 for Wafer B in in the flux range between $\phi = 2.37 \times 10^{16}$ and $\phi = 1.02 \times 10^{17}$ cm^{-2}s^{-1}. In this case we clearly observe the steeper injection dependence (larger ratio between high and low injection lifetime) in the grains as compared to the regions dominated by recombination from grain boundaries dislocation clusters. More details and features can also be seen in the low lifetime regions which are not visible in the conventional lifetime image shown in Figure 4.

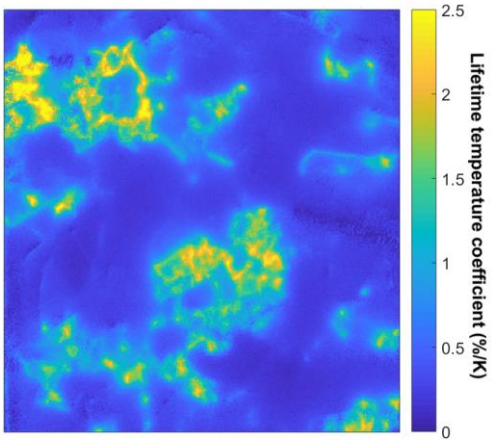

Figure 7. Map of the temperature coefficient of the carrier lifetime at constant flux of $\phi = 1.02 \times 10^{17}$cm^{-2}s^{-1}, measured in % change per K in the temperature range between 25 ˚C and 75 ˚C. The temperature coefficient map is calculated based on data from Wafer B.

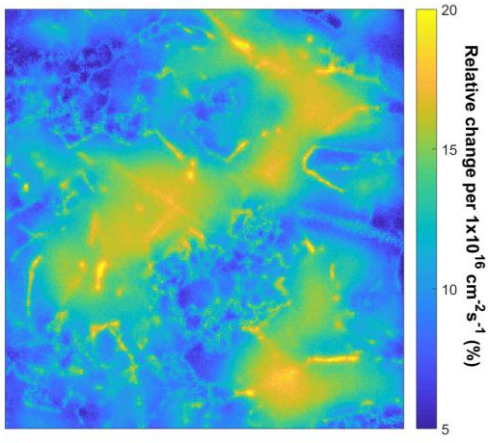

Figure 8. Map of the relative change in the lifetime with increasing photon flux, in the range between $\phi = 2.37 \times 10^{16}$ and $\phi = 1.02 \times 10^{17}$ cm^{-2}s^{-1}, calculated based on data from Wafer B.

Lastly, the data can be used to generate lifetime images with at a constant Δn at every point of the image. Conventional PL lifetime images are taken at a constant generation rate, and areas of different effective lifetime will therefore be at different injection levels, according to the steady state relation $\Delta n = G \times \tau_{eff}$. By acquiring and storing a range of images at different generation rates …

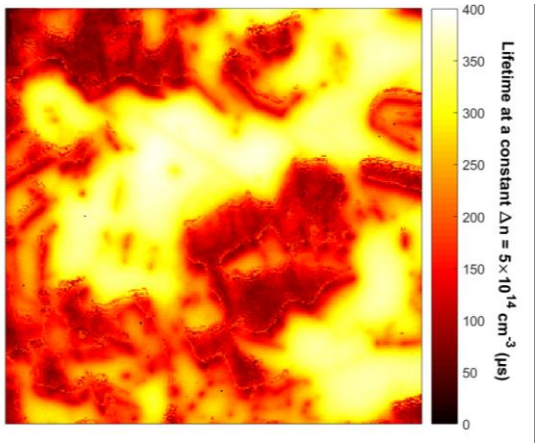

Figure 9. Carrier lifetime image at a constant injection level of $\Delta n = 5 \times 10^{14}$ cm^{-3}, instead of the conventional image taken at a constant generation rate. The image is calculated from data from Wafer B by interpolating the value at each pixel between images taken at different excitation intensities.

5. Summary and further work

5.1 Summary of results

In this paper we have demonstrated a method for performing temperature- and injection level dependent lifetime spectroscopy with high lateral resolution based on automated acquisition and analysis of a large number of PL images taken under different conditions. Two passivated, neighboring HPMC silicon wafers were investigated, one in the as-cut state and one which had received a simulated solar cell process including phosphorous diffusion gettering and hydrogenation during a high temperature firing step. One in-grain region and one region dominated by dislocations clusters were studied in each of the two wafers. For each region the contributions from one or two SRH defects were isolated by linearization and fitting of the injection-dependent SRH lifetime curves at each temperature. The defect energy level E_t and capture cross section ratio k for each defect was determined from the points of intersection between the defect parameter solution surfaces (DPSS) for each temperature. We find that two defects are needed to describe the observed behavior in both regions of the as-cut wafer, and one of the observed defects in the dislocated region corresponds well with previously reported values for iron-boron complexes. One other clearly defined defect is also observed in this region, which could possibly be interstitial iron Fe_i. For the wafer after solar cell processing the in-grain region was described very well using a single, unidentified SRH defect located deep in the band gap, with $k = 10 \pm 1$. In the region of this wafer dominated by dislocation clusters, two defects are needed to explain the results, here we observe one shallow defect within 0.21 eV from the band edge and one deep defect with $k = 25 \pm 2$. The defect parameters for the latter defect was also observed in the in-grain regions of the as-cut wafer.

In addition to the TIDLS analysis, we demonstrate several image visualizations of the measured lifetime data, illustrating the lateral distribution of both the temperature and injection dependence of the carrier lifetime. These include images of the lifetime temperature coefficient, the relative change in lifetime with increasing flux and lifetime images at a constant injection level, generated by interpolating the values at each pixel between images taken at a given temperature.

5.2 Further work

The experimental setup and analysis tools used in this paper is still under development, and several further changes could be introduced to improve the accuracy of the obtained results. Firstly, smearing of the images due to lateral carrier diffusion will influence the results, this limiting how local the defect analysis can be. Post-process image correction to correct for carrier diffusion, e.g. as presented in Ref. [35] could therefore be utilized to mitigate this. Furthermore, we aim to improve the calibration procedure in the hope to avoid the observed uncertainties related to the injection dependence of the calibration constant by implementing a true steady state photoconductance measurement in the PL setup, as discussed in Ref. [36]. We are also currently implementing measures to further increase the injection range in low injection in order to improve the robustness of determination of $\boldsymbol{k}$. Lastly, further sensitivity analysis of the TIDLS data is also useful to quantify the accuracy of the obtained defect parameters. When these measures are in place, the tool demonstrated here could be used to generate full maps of the defect parameters obtained from the two-defect fit, together with the fit quality in each pixel of the image. The approach investigated in this paper is thus not without issues, but it is still found to be a powerful technique for local analysis of the dominant recombination mechanisms in Si wafers using commonly used and commercially available tools for Si solar cell research.

Acknowledgements

Funding for this work was partly provided through the EnergiX programme of the Norwegian Research Council, project number 268027 - Crucibles for next generation high quality silicon solar cells (CruGenSi)

References

[1] J. D. Murphy, K. Bothe, M. Olmo, V. V Voronkov, and R. J. Falster, "The effect of oxide precipitates on minority carrier lifetime in p-type silicon," *J. Appl. Phys.*, vol. 110, no. 5, p. 53713, Sep. 2011.

[2] H. Angelskår, R. Søndenå, M. S. Wiig, and E. S. Marstein, "Characterization of Oxidation-Induced Stacking Fault Rings in Cz Silicon: Photoluminescence Imaging and Visual Inspection After Wright etch," *Energy Procedia*, vol. 27, pp. 160–166, 2012.

[3] S. Bernardini *et al.*, "Nano-XRF Analysis of Metal Impurities Distribution at PL Active Grain Boundaries During mc-Silicon Solar Cell Processing," *IEEE J. Photovoltaics*, vol. 7, no. 1, pp. 244–249, 2017.

[4] H. C. Sio *et al.*, "Recombination sources in p-type high performance multicrystalline silicon," *Jpn. J. Appl. Phys.*, vol. 56, no. 8S2, p. 08MB16, 2017.

[5] B. Hallam *et al.*, "Recent insights into boron-oxygen related degradation: Evidence of a single defect," *Sol. Energy Mater. Sol. Cells*, vol. 173, pp. 25–32, 2017.

[6] R. Søndenå and M. S. Wiig, "Evolution of the light sensitive defects in high performance multicrystalline silicon wafers," *J. Appl. Phys.*, vol. 125, no. 8, p. 85701, Feb. 2019.

[7] T. Niewelt, F. Schindler, W. Kwapil, R. Eberle, J. Schön, and M. C. Schubert, "Understanding the light-induced degradation at elevated temperatures: Similarities between multicrystalline and floatzone p-type silicon," *Prog. Photovoltaics Res. Appl.*, vol. 26, no. 8, pp. 533–542, Aug. 2018.

[8] M. A. Green *et al.*, "Solar cell efficiency tables (Version 53)," *Prog. Photovoltaics Res. Appl.*, vol. 27, no. 1, pp. 3–12, Jan. 2019.

[9] M. Syre, S. Karazhanov, B. R. Olaisen, A. Holt, and B. G. Svensson, “Evaluation of possible mechanisms behind P gettering of iron,” *J. Appl. Phys.*, vol. 110, no. 2, p. 024912, 2011.
[10] M. S. Wiig, K. Adamczyk, H. Haug, K. E. Ekstrøm, and R. Søndenå, “The Effect of Phosphorus Diffusion Gettering on Recombination at Grain Boundaries in HPMC-Silicon Wafers,” *Energy Procedia*, vol. 92, pp. 886–895, Aug. 2016.
[11] M. Rinio, A. Yodyungyong, S. Keipert-Colberg, D. Borchert, and A. Montesdeoca-Santana, “Recombination in ingot cast silicon solar cells,” *Phys. status solidi*, vol. 208, no. 4, pp. 760–768, Apr. 2011.
[12] H. C. Sio, S. P. Phang, T. Trupke, and D. Macdonald, “Impact of Phosphorous Gettering and Hydrogenation on the Surface Recombination Velocity of Grain Boundaries in p-Type Multicrystalline Silicon,” *IEEE J. Photovoltaics*, vol. 5, no. 5, pp. 1357–1365, 2015.
[13] S. Rein, *Lifetime Spectroscopy - A Method of Defect Characterization in Silicon for Photovoltaic Applications*. Springer-Verlag, 2005.
[14] A. E. Morishige *et al.*, “Lifetime Spectroscopy Investigation of Light-Induced Degradation in p-type Multicrystalline Silicon PERC,” *IEEE J. Photovoltaics*, vol. 6, no. 6, pp. 1466–1472, 2016.
[15] C. Vargas *et al.*, “Recombination parameters of lifetime-limiting carrier-induced defects in multicrystalline silicon for solar cells,” *Appl. Phys. Lett.*, vol. 110, no. 9, p. 92106, Feb. 2017.
[16] J. A. Giesecke, M. C. Schubert, F. Schindler, and W. Warta, “Harmonically Modulated Luminescence: Bridging Gaps in Carrier Lifetime Metrology Across the PV Processing Chain,” *Photovoltaics, IEEE Journal of*, vol. 5, no. 1. pp. 313–319, 2015.
[17] L. E. Mundt *et al.*, “Spatially Resolved Impurity Identification via Temperature- and Injection-Dependent Photoluminescence Imaging,” *Photovoltaics, IEEE Journal of*, vol. 5, no. 5. pp. 1503–1509, 2015.
[18] J. Schön *et al.*, “Identification of lifetime limiting defects by temperature- and injection-dependent photoluminescence imaging,” *J. Appl. Phys.*, vol. 120, no. 10, p. 105703, Sep. 2016.
[19] M. S. Wiig, H. Haug, R. Søndenå, and E. S. Marstein, “Identifying recombination parameters by injection-dependent lifetime spectroscopy on mc-silicon based on photoluminescence imaging,” *AIP Conf. Proc.*, vol. 1999, no. 1, p. 130017, Aug. 2018.
[20] S. Diez, S. Rein, T. Roth, and S. W. Glunz, “Cobalt related defect levels in silicon analyzed by temperature- and injection-dependent lifetime spectroscopy,” *J. Appl. Phys.*, vol. 101, no. 3, p. 33710, Feb. 2007.
[21] S. Rein and S. W. Glunz, “Electronic properties of interstitial iron and iron-boron pairs determined by means of advanced lifetime spectroscopy,” *J. Appl. Phys.*, vol. 98, no. 11, p. 113711, Dec. 2005.
[22] A. Inglese, J. Lindroos, H. Vahlman, and H. Savin, “Recombination activity of light-activated copper defects in p-type silicon studied by injection- and temperature-dependent lifetime spectroscopy,” *J. Appl. Phys.*, vol. 120, no. 12, p. 125703, Sep. 2016.
[23] A. Richter, S. W. Glunz, F. Werner, J. Schmidt, and A. Cuevas, “Improved quantitative description of Auger recombination in crystalline silicon,” *Phys. Rev. B*, vol. 86, no. 16, p. 165202, Oct. 2012.
[24] J. Murphy, K. Bothe, R. Krain, V. Voronkov, and R. Falster, *Parameterisation of injection-dependent lifetime measurements in semiconductors in terms of Shockley-Read-Hall statistics: An application to oxide precipitates in silicon*, vol. 111. 2012.
[25] H. Haug, R. Søndenå, M. S. Wiig, and E. S. Marstein, “Temperature dependent photoluminescence imaging calibrated by photoconductance measurements,” *Energy Procedia*, vol. 124, pp. 47–52, Sep. 2017.
[26] T. Trupke *et al.*, “Temperature dependence of the radiative recombination coefficient of intrinsic crystalline silicon,” *J. Appl. Phys.*, vol. 94, no. 8, pp. 4930–4937, Oct. 2003.
[27] Z. Hameiri, M. K. Juhl, R. Carlaw, and T. Trupke, “Spatially resolved lifetime spectroscopy from temperature-dependent photoluminescence imaging,” *Photovoltaic Specialist Conference (PVSC), 2015 IEEE 42nd*. pp. 1–3, 2015.
[28] J. M. Dorkel and P. Leturcq, “Carrier mobilities in silicon semi-empirically related to temperature, doping and injection level,” *Solid. State. Electron.*, vol. 24, no. 9, pp. 821–825, 1981.
[29] Sinton-Instruments, “WCT-120TS product note.” [Online]. Available: http://www.sintoninstruments.com/PDFs/Sinton-WCT-120TS-product-note.pdf.
[30] H. C. Sio, S. P. Phang, T. Trupke, and D. Macdonald, “An accurate method for calibrating photoluminescence-based lifetime images on multi-crystalline silicon wafers,” *Sol. Energy Mater. Sol. Cells*, vol. 131, pp. 77–84, 2014.
[31] S. Herlufsen, J. Schmidt, D. Hinken, K. Bothe, and R. Brendel, “Photoconductance-calibrated photoluminescence lifetime imaging of crystalline silicon,” *Phys. status solidi - Rapid Res. Lett.*, vol. 2, no. 6, pp. 245–247, Dec. 2008.
[32] D. Macdonald, R. a. Sinton, and A. Cuevas, “On the use of a bias-light correction for trapping effects

in photoconductance-based lifetime measurements of silicon," *J. Appl. Phys.*, vol. 89, no. 5, p. 2772, 2001.

[33] G. Stokkan, Y. Hu, Ø. Mjøs, and M. Juel, "Study of evolution of dislocation clusters in high performance multicrystalline silicon," *Sol. Energy Mater. Sol. Cells*, vol. 130, pp. 679–685, 2014.

[34] R. Eberle, S. T. Haag, I. Geisemeyer, M. Padilla, and M. C. Schubert, "Temperature Coefficient Imaging for Silicon Solar Cells," *IEEE J. Photovoltaics*, vol. 8, no. 4, pp. 930–936, 2018.

[35] S. P. Phang, H. C. Sio, and D. Macdonald, "Carrier de-smearing of photoluminescence images on silicon wafers using the continuity equation," *Appl. Phys. Lett.*, vol. 103, no. 19, p. 192112, 2013.

[36] S. T. Kristensen *et al.*, "A High-Accuracy Calibration Method for Temperature Dependent Photoluminescence Imaging (to be published)," in *AIP Conference Proceedings*, 2019.